J. Fluid Mech. (2018), *vol.* 837, *pp.* 320–340.
doi:10.1017/jfm.2017.853

Transport of anisotropic particles under waves

Michelle H. DiBenedetto[1],†, Nicholas T. Ouellette[1] and Jeffrey R. Koseff[1]

[1]The Bob and Norma Street Environmental Fluid Mechanics Laboratory, Department of Civil and Environmental Engineering, Stanford University, Stanford, CA 94305, USA

(Received 28 April 2017; revised 19 September 2017; accepted 18 November 2017)

Using a numerical model, we analyse the effects of shape on both the orientation and transport of anisotropic particles in wavy flows. The particles are idealized as prolate and oblate spheroids, and we consider the regime of small Stokes and particle Reynolds numbers. We find that the particles preferentially align into the shear plane with a mean orientation that is solely a function of their aspect ratio. This alignment, however, differs from the Jeffery orbits that occur in the residual shear flow (that is, the Stokes drift velocity field) in the absence of waves. Since the drag on an anisotropic particle depends on its alignment with the flow, this preferred orientation determines the effective drag on the particles, which in turn impacts their net downstream transport. We also find that the rate of alignment of the particles is not constant and depends strongly on their initial orientation; thus, variations in initial particle orientation result in dispersion of anisotropic-particle plumes. We show that this dispersion is a function of the particle's eccentricity and the ratio of the settling and wave time scales. Due to this preferential alignment, we find that a plume of anisotropic particles in waves is on average transported farther but dispersed less than it would be if the particles were randomly oriented. Our results demonstrate that accurate prediction of the transport of anisotropic particles in wavy environments, such as microplastic particles in the ocean, requires the consideration of these preferential alignment effects.

Key words: multiphase and particle-laden flows, particle/fluid flow, surface gravity waves

1. Introduction

In a vast array of both industrial and natural situations, fluid flows transport small particulate matter that is not neutrally buoyant. Due to its widespread applications, then, the question of how such 'weakly inertial' particles are transported in both turbulent (Guha 2008) and laminar (Leal 1980) flows has been a very active topic of research. The dynamics of such particles is highly complex, because they do not in general move in the same way as an equivalently sized fluid element would – they experience different forces, and may even eventually settle out. For spherical inertial particles, the response time scale of the particles relative to the time scale of the smallest fluid motions, a ratio known as the Stokes number, dictates the degree to which particles follow the flow. For nearly inertialess particles (that is, those

† Email address for correspondence: mdiben@stanford.edu

with small Stokes and particle Reynolds numbers), these differences may be small when evaluating velocities at a single instant; but when predicting long-time particle transport, there may be an integrated effect that can result in larger discrepancies even in this limit (Ouellette, O'Malley & Gollub 2008).

When finite-sized particles are additionally not spherical, their dynamics can be further influenced by orientation-dependent lift and drag forces. Thus, the way that the shape of particles couples to their rotational and translational dynamics is an emerging area of interest (Andersson & Soldati 2013; Voth & Soldati 2017). Much of this research has explored the rotational dynamics of rods and prolate spheroids in turbulence; for examples, see Shin & Koch (2005), Pumir & Wilkinson (2011), Parsa *et al.* (2012), Ni, Ouellette & Voth (2014). A growing body of work, however, has addressed a broader spectrum of anisotropic-particle shapes, with again focus on characterizing particle rotational dynamics in isotropic turbulence via models (Klett 1995) and simulations (Byron *et al.* 2015) and in shear flows (Challabotla, Zhao & Andersson 2015*a*). Inertia is often neglected in these simulations, which led Einarsson, Angilella & Mehlig (2014) to analyse how weak inertia may affect some of these orientational dynamics findings. This focus on rotation is partly due to the symmetries of isotropic turbulence, so that long-time transport is not necessarily expected to be affected by particle orientation, and to the fact that the rotational and translational degrees of freedom for an anisotropic but non-chiral particle are not expected to be coupled (Brenner 1964).

In many cases, however, there is the possibility that the flow itself may break this symmetry and couple particle shape to transport. Our particular motivating case is that of the fate of microplastic particles in the ocean. Microplastics, a persistent and growing source of contamination in our oceans (Van Sebille *et al.* 2015), are typically defined to be small irregularly shaped plastic particles with length scales of less than 5 mm. Their most typical forms are elongated and fibrous, flat and planar fragments (Chubarenko *et al.* 2016), or nearly spherical pellets (Ryan *et al.* 2009). Thus, to a good approximation, they can be idealized as particles along the spheroidal spectrum, from discs to spheres to rods. Such an approximation is additionally justified given that simplifying complex shapes to spheroids has been proven as an effective modelling technique by Bretherton (1962). Microplastic mass densities are close to that of water, but may be either positively or negatively buoyant. Most efforts to model microplastic transport in the ocean, however, treat the particles as tracers (Maximenko, Hafner & Niiler 2012), potentially with a superimposed constant settling velocity (Kukulka *et al.* 2012), or neglect any effects of their shape and instead prescribe only bulk properties to the modelled particles (Beron-Vera, Olascoaga & Lumpkin 2016). Although this latter approach may be more accurate than treating microplastics as pure flow tracers, neglecting particle shape effects has been shown to result in errors in predictions of anisotropic-particle transport (Broday *et al.* 1997).

Most plastic pollution in the ocean is land sourced, and many delicate ecosystems reside near shorelines. Thus, understanding the transport of microplastics in the near-shore environment is a key environmental problem. The transport of scalars in the near-shore, coastal zone is controlled by phenomena such as wind waves, turbulence, Langmuir cells, longshore currents, rip currents and tidal currents. These complex and interacting hydrodynamic phenomena influence transport in these areas. Here, however, we simplify the problem and examine one simple but ubiquitous aspect of the near-shore environment: surface gravity waves. While linear wave theory predicts that fluid elements trace orbits as the wave passes, surface gravity waves

also generate a mean Lagrangian current or Stokes drift (Stokes 1851). This induced current has well-studied effects on large-scale transport and mixing processes in the ocean as it interacts with other forces. For example, the Coriolis–Stokes forcing can induce opposing flow (Hasselmann 1970), and the Stokes vortex force describes how wind shear produces Langmuir circulation (Leibovich 1983; McWilliams, Sullivan & Moeng 1997). When diffusion of particles is also included, a non-zero mean drift velocity appears even in the case where classical Stokes drift would vanish; this has been termed stochastic Stokes drift (Jansons & Lythe 1998). Stokes drift has also been shown to be an important mechanism for modelling the transport of microplastics in the coastal oceans (Isobe *et al.* 2014). Less is known, however, about how weakly inertial, anisotropic particles behave in these wavy flows.

The mean transport of particles in internal gravity waves was studied by Grinshpun *et al.* (2000), who examined Stokes drag on particles that were essentially inertialess. However, as discussed above, inertial particles feel other forces as well. Previous studies that modelled the transport of finite-sized spherical particles under surface gravity waves found that added mass must be included (Eames 2008) as well as other inertial effects (Santamaria *et al.* 2013). The properties of the waves themselves can also lead to different results (Bakhoday-Paskyabi 2015). Even though these models are very simple, they show that inertial particle transport in waves is both non-trivial and not well understood.

Here, we bring together these various threads of research and study the effects of shape and weak inertia on the orientation and transport of particles in wavy flows. We conducted numerical simulations of anisotropic, inertialess and weakly inertial spheroids in an analytically specified wave field. We find that the particles adopt preferential orientations relative to the wave propagation direction that are purely a function of their aspect ratio; and that this preferential alignment in turn leads to differences in the downstream transport of the particles. Thus, the interaction of the flow field and the particle dynamics leads to a coupling between the particle shape and their net transport. We also find that the rate of approach to this preferred alignment depends on the initial particle orientation, so that a plume of randomly oriented anisotropic particles will experience dispersion as it is advected downstream. Our results demonstrate that particle shape is a key component for predicting transport in wavy flows and should be included in models of the dispersal of oceanic microplastics.

We begin below in § 2 by describing our model for both the particles and the flow. In § 3, we present our results, focusing separately on the particle orientation, transport and dispersion. We also consider the contribution of the wavy oscillation in addition to the residual Stokes drift velocity field. Finally, in § 4, we summarize our results and discuss the potential contributions of effects we have not considered in our model.

2. Methodology

2.1. *Particle model*

We simulated particle trajectories using a point-particle approach to isolate the effects of particle shape on transport. The modelled particles are spheroids, and are described by d_s, the diameter of the equivalent sphere with the same volume as the spheroid, and $\mathcal{E}$, the eccentricity. We define $\mathcal{E}$ as $(\lambda^2 - 1)/(\lambda^2 + 1)$, where λ is the aspect ratio and is given by the ratio a/b, where a is the length along the particle's axis of symmetry and b is the length of one of the orthogonal axes, as shown in figure 1. We considered both oblate ($\mathcal{E} < 0$) and prolate ($\mathcal{E} > 0$) spheroids. Note that $\mathcal{E} = 0$ for a sphere, and that the limiting cases of $\mathcal{E} \to \pm 1$ correspond to rods and discs, respectively.

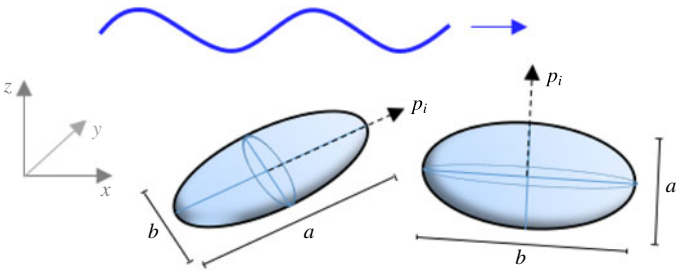

FIGURE 1. (Colour online) Characteristics of particles used in the simulations. Both a prolate and oblate spheroidal particle and their corresponding diameters and symmetry axis in the coordinate system are shown. The waves lie in the x–z plane and move in the positive x direction; they are not shown to scale. The particle's orientation is described by the unit vector p_i, which lies along the particle's axis of symmetry.

We ran simulations both with and without consideration of particle inertia. As described below, neglecting inertia allows us to isolate the interaction between the wave-driven flow and the particle orientation, whereas simulations with inertia allow the characterization of the effect of the orientation on particle transport.

In the inertialess limit, the particles follow fluid-element trajectories, although their orientation gives them additional degrees of freedom. Their rotation is governed by Jeffery's (1922) equation for a spheroid, given by

$$\dot{p}_i = \Omega_{ij} p_j + \mathcal{E}(S_{ij} p_j - p_i p_j S_{jl} p_l), \tag{2.1}$$

where Ω_{ij} and S_{ij} are the anti-symmetric and symmetric parts of the fluid velocity gradient tensor and p_i is a unit vector pointing along the particle's axis of symmetry, as shown in figure 1.

When particle inertia is included, both the orientation and trajectory of the particle must be considered, since the particles no longer follow the flow. We assumed one-way coupling between the fluid and the particles, so that there is no back reaction of the particles on the flow; we also ignored particle–particle interactions and collisions. We also only considered the low particle Reynolds number regime. We define the particle Reynolds number Re_p to be $Re_p = |v - u|d/\nu$, where v is the particle velocity, u is the fluid velocity at the centre of the particle, d is the longest length scale of the particle and ν is the kinematic viscosity of the fluid, and we fix $Re_p < 1$. To compute the particle trajectories, we integrate a modified form of the Maxey–Riley (1983) equation. This equation was originally derived for the unsteady motion of spherical particles with $Re_p \ll 1$; thus, we have modified some of the terms to account for non-spherical effects. In wavy flows like those we consider here, added-mass effects were shown to be important for spherical particles (Eames 2008) (for a more general scaling of the Maxey–Riley equation, see Ling, Parmar & Balachandar (2013)); thus, we keep added mass here. We neglect, however, the Basset history force since the particles are small, and the Faxén corrections and the Saffman lift force since they are negligible given our flow parameters.

With these simplifications, the equation of motion for each particle is

$$\frac{\mathrm{d}v_i}{\mathrm{d}t} = \frac{1}{\mathcal{B}}\frac{\mathrm{D}u_i}{\mathrm{D}t} - \frac{1}{\mathcal{B}} C_{ij}^m \frac{\mathrm{d}}{\mathrm{d}t}(v_j - u_j) - 18\frac{\nu}{\mathcal{B} d_s^2} K_{ij}(v_j - u_j) - \left(1 - \frac{1}{\mathcal{B}}\right) g\delta_{i3}, \tag{2.2}$$

where the terms on the right-hand side are, in order, the advection, added mass, Stokes drag and buoyancy forces. Here, C_{ij}^m is a tensor of added mass coefficients, $\mathcal{B} = \rho_p/\rho_f$ is the density ratio between the particle and the fluid, g is the acceleration due to gravity and K_{ij} is the resistance tensor (Brenner 1964).

We calculate the full, anisotropic added mass tensor in these simulations in order to fully quantify the effects of shape. In a frame aligned with the body axes of the particle, the components of the added mass tensor C_{ij}^m are given in terms of non-dimensional factors α_0, β_0 and γ_0, (Lamb 1945) defined as

$$C_{11}^{m\,\prime} = \frac{\alpha_0}{2-\alpha_0}, \tag{2.3a}$$

$$C_{22}^{m\,\prime} = \frac{\beta_0}{2-\beta_0}, \tag{2.3b}$$

$$C_{33}^{m\,\prime} = \frac{\gamma_0}{2-\gamma_0}, \tag{2.3c}$$

where the prime indicates that these components are those in the body-axis frame where C_{ij}^m is diagonal and the x'-axis is along the particle's axis of symmetry. The dimensionless factors are derived as functions of the 'eccentricity of the meridian' in Lamb (1945), and were later reported for prolate spheroids by Gallily & Cohen (1979) and for oblate spheroids by Siewert *et al.* (2014) in terms of aspect ratio. For prolate spheroids, $\lambda > 1$:

$$\alpha_0 = \frac{1}{(\lambda^2-1)^{3/2}}\left(2(\lambda^2-1)^{1/2} + \lambda \ln\left(\frac{\lambda-(\lambda^2-1)^{1/2}}{\lambda+(\lambda^2-1)^{1/2}}\right)\right), \tag{2.4a}$$

$$\beta_0 = \gamma_0 = \frac{1}{2(\lambda^2-1)^{3/2}}\left(2\lambda^2(\lambda^2-1)^{1/2} + \lambda \ln\left(\frac{\lambda-(\lambda^2-1)^{1/2}}{\lambda+(\lambda^2-1)^{1/2}}\right)\right), \tag{2.4b}$$

and for oblate spheroids, $\lambda < 1$:

$$\alpha_0 = \frac{\lambda}{(1-\lambda^2)^{3/2}}(2\lambda \tan^{-1}(\lambda(1-\lambda^2)^{-1/2}) - \lambda\pi + 2(1-\lambda^2)^{1/2}), \tag{2.5a}$$

$$\beta_0 = \gamma_0 = -\frac{\lambda}{2(1-\lambda^2)^{3/2}}(2\tan^{-1}(\lambda(1-\lambda^2)^{-1/2}) - \pi + 2\lambda(1-\lambda^2)^{1/2}). \tag{2.5b}$$

The resistance tensor K_{ij} accounts for the variation of the drag on the particle as it rotates and presents different cross-sections to the flow. Just as with C_{ij}^m, K_{ij} is diagonal in the body-axis frame of the particle. To compute it, we use the expressions for its eigenvalues, or drag correction factors, as derived by Oberbeck (1876) and reported in Loth (2008); the eigenvalue associated with the axis of symmetry is given by

$$f_a = \begin{cases} \dfrac{(4/3)\lambda^{-1/3}(1-\lambda^2)}{\lambda - \dfrac{(2\lambda^2-1)\ln(\lambda+\sqrt{\lambda^2-1})}{\sqrt{\lambda^2-1}}}, & \text{if } \lambda > 1 \\ \dfrac{(4/3)\lambda^{-1/3}(1-\lambda^2)}{\lambda + \dfrac{(1-2\lambda^2)\cos^{-1}(\lambda)}{\sqrt{1-\lambda^2}}}, & \text{if } \lambda < 1 \end{cases} \tag{2.6}$$

and the eigenvalues for the other two directions are given by

$$f_b = \begin{cases} \dfrac{(8/3)\lambda^{-1/3}(\lambda^2-1)}{\lambda + \dfrac{(2\lambda^2-3)\ln(\lambda+\sqrt{\lambda^2-1})}{\sqrt{\lambda^2-1}}}, & \text{if } \lambda > 1 \\ \dfrac{(8/3)\lambda^{-1/3}(\lambda^2-1)}{\lambda - \dfrac{(3-2\lambda^2)\cos^{-1}(\lambda)}{\sqrt{1-\lambda^2}}}, & \text{if } \lambda < 1. \end{cases} \tag{2.7}$$

Both $C_{ij}^{m'}$ and K'_{ij} then need to be rotated from the body-axis frame into the flow's frame of reference to evaluate the right-hand side of equation (2.2). For example, $K_{ij} = R_{pi}K'_{pq}R_{qj}$, where R_{ij} is the rotation matrix that rotates from the flow's reference frame to the current direction of the orientation vector p_i. We note that this formulation allows for lift forces (that is, forces orthogonal to the particle's symmetry axis) on the particle as well as drag.

To characterize how well the particle responds to the flow, the Stokes number St is typically used. In our case, it is calculated as the ratio of τ_p, the relaxation time of the particle, to the wave period T. The relaxation time of a spherical particle in Stokes flow is given by $\tau_p^s = \mathcal{B}d_s^{\,2}/18\nu$, but is more difficult to define for an anisotropic particle since the particle's resistance varies with its relative orientation to the flow. We use parameterizations that account for the resistance equally in all directions, as shown below for both a prolate spheroid (Shapiro & Goldenberg 1993) and an oblate spheroid (Zhao *et al.* 2015), as also reported in Voth & Soldati (2017). We note that both of these parameterizations appropriately return to the spherical limit for $\lambda = 1$. Here, we have rewritten them in terms of the spherical relaxation time to make them more clear. Based on volume equivalence, the spheroid principle axes have lengths $a = d_s\lambda^{2/3}$, and $b = d_s\lambda^{-1/3}$, and so the spheroid relaxation time can be expressed as that of an equivalent sphere multiplied by a correction factor k_τ. Therefore, $\tau_p = k_\tau\tau_p^s$, where

$$k_\tau = \begin{cases} \lambda^{1/3}\left(\dfrac{\ln(\lambda+\sqrt{\lambda^2-1})}{\sqrt{\lambda^2-1}}\right), & \text{if } \lambda > 1 \\ \lambda^{-2/3}\left(\dfrac{\pi - 2\tan^{-1}(\lambda(1-\lambda^2)^{-1/2})}{2\sqrt{1-\lambda^2}}\right), & \text{if } \lambda < 1. \end{cases} \tag{2.8}$$

We plot the value of k_τ for all $\mathcal{E}$ in figure 2 to demonstrate how the relaxation time varies with shape. Prolate ellipsoids have very similar relaxation times to a sphere, except in the very high-aspect-ratio rod limit where their relaxation time goes to zero since the expressions in (2.8) are based on the minor axis length scale b, which vanishes in the rod limit. In the disc limit, b becomes very large, which is why the disc relaxation time rapidly increases. This plot indicates that there should be a noticeable difference in how discs, ellipsoids and spheres respond to the flow. As shown below, however, our results do not always show such a sensitivity; thus, we caution that St is not necessarily the best parameter for evaluating shape effects.

For the slightly inertial particles we consider, with small St and Re_p, we calculate the rotation using Euler's equation of rigid body motion in the frame of reference of the particle, given by

$$I'_{ij}\frac{\mathrm{d}\omega'_j}{\mathrm{d}t} + \epsilon_{ijk}\omega'_j I'_{kl}\omega'_l = M'_i, \tag{2.9}$$

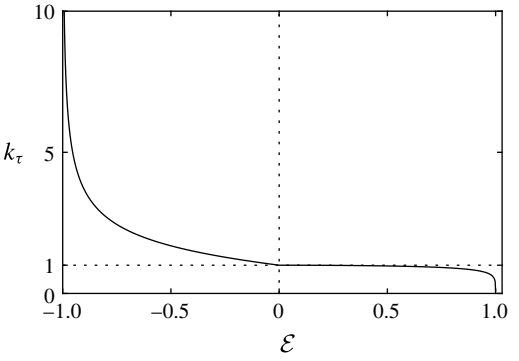

FIGURE 2. Particle Stokesian relaxation time correction k_τ versus eccentricity for both oblate and prolate spheroids. The dotted lines intersect at the spherical case, the point (0, 1).

where ω_i is the rate of angular rotation of the particle, related to the orientation by $\dot{p}_i = \epsilon_{ijk}\omega_j p_k$, ϵ_{ijk} is the Levi-Civita symbol, I_{ij} is the particle's moment of inertia tensor and M_i, the torques on the particle as derived by Jeffery (1922), are

$$M_i = \begin{bmatrix} \dfrac{32\pi\mu(\Omega_{23} - \omega_1)}{(3(\beta_0 + \gamma_0))} \\ \dfrac{16\pi\mu((b^2 - a^2)S_{13} + (b^2 + a^2)(\Omega_{13} - \omega_2))}{(3(b^2\gamma_0^2 + a^2\alpha_0^2))} \\ \dfrac{16\pi\mu((a^2 - b^2)S_{12} + (b^2 + a^2)(\Omega_{12} - \omega_3))}{(3(b^2\beta_0^2 + a^2\alpha_0^2))} \end{bmatrix}. \tag{2.10}$$

Here, μ is the dynamic viscosity of the fluid. We neglect rotational added mass; it vanishes identically for a sphere and is still relatively small in the context of our parameter regime. If included, it would effectively increase the particle's moment of inertia in the non-spherical case, but would not affect our results qualitatively.

2.2. *Flow*

We describe the flow analytically using linear wave theory. This theory applies to waves with low wave steepness, requiring $kA \leqslant 0.33$, where A is the wave amplitude and k is the wavenumber, related to the wavelength L by $k = 2\pi/L$. Wavy flow described by linear wave theory is irrotational, so the first term of equation (2.1) vanishes in our flow, as do all the Ω_{ij} terms in equation (2.10). We primarily consider the case of waves over an infinite depth h to remove any depth dependence. We note that we also tested finite-depth waves and found similar results. In the deep-water limit, where $kh \gg 1$ and the flow is restricted to two dimensions, the velocity field is described in x–y–z space by

$$\boldsymbol{u}(x, z, t) = \omega A \mathrm{e}^{kz}(\cos(kx - \omega t)\hat{\boldsymbol{e}}_x + \sin(kx - \omega t)\hat{\boldsymbol{e}}_z), \tag{2.11}$$

where ω is the wave frequency and $\hat{\boldsymbol{e}}_i$ is a unit vector in the i direction. The wavenumber and frequency are related through the deep-water dispersion relation $\omega = \sqrt{gk}$ and the wave period $T = 2\pi/\omega$. In this velocity field, the mean Eulerian

flow is zero everywhere; however, the Lagrangian mean flow produces a residual horizontal transport in the direction of the waves, known as Stokes drift. The Stokes drift velocity for deep-water waves is only a function of depth, and is given by

$$\boldsymbol{u}_s(z) = \omega k A^2 \mathrm{e}^{2kz} \hat{\boldsymbol{e}}_x. \tag{2.12}$$

As our wavy flows are irrotational, there is no vorticity with which the particles can align. However, previous work in isotropic turbulence and shear flows has found that low Stokes number anisotropic particles will tend to align into the shear plane for both oblate (Challabotla *et al.* 2015*a*) and prolate particles (Mortensen *et al.* 2008). In the creeping shear flow with inertialess spheroids described by Jeffery (1922), the particles undergo any number of closed periodic orbits that are dependent on initial condition.

In our simulations, we do not assume anything about the particles' initial orientations, as microplastics do not necessarily enter the ocean from a localized point source. Instead, to keep our results general and fully explore the interplay of shape and orientation, we vary the initial orientation, sampling uniformly on the unit sphere. This is done both to capture some of the variability that would occur in real physical flows where the initial orientation may be unconstrained, and to isolate the effects solely due to particle orientation and wave interactions. We describe the orientation in spherical coordinates in the wave reference frame, labelling the azimuthal angle θ and the polar angle ϕ. In order to generate a distribution of random points uniformly distributed on the unit sphere, we first define X and Y as uniform random variables with values between 0 and 1 and then set $\theta = 2\pi X$ and $\phi = \sin^{-1}(2Y - 1)$. Due to symmetry, we need only to sample the initial orientations of p_i in the ranges $0 \leqslant \phi < \pi$ and $0 \leqslant \theta < \pi/2$.

The particles are initialized with the fluid velocity plus their corresponding settling velocity. The initial settling velocity $w_p(t=0)$ is given by

$$w_p(t=0) = \frac{g d_s^2 (\mathcal{B} - 1)}{18 \nu K_{33}|_{(t=0)}}, \tag{2.13}$$

and is found by evaluating the steady-state velocity of the particle settling in quiescent fluid with $\boldsymbol{u} = 0$, leaving only the drag term and the gravity term in (2.2).

We move through our parameter space by manipulating the dimensionless parameters kA, $\mathcal{B}$, $\mathcal{E}$ and St. For the analysis presented here, we use a set of 380 different combinations of these values, including a range of both positive and negative eccentricities. The Stokes number was varied between zero and unity. The ratio of the Stokes drift velocity to the particle settling velocity was varied as well; this was done by manipulating the density ratio $\mathcal{B}$, the particle size d_s and the wave amplitude A.

3. Results

3.1. *Orientation*

In the limit of vanishing particle inertia, we find that the particles rotate to a time-averaged alignment that is independent of the flow and only a function of their shape. This behaviour contrasts with the infinite number of Jeffery orbits that exist in a shear flow that are solely dependent on initial condition. No matter the particle's initial orientation in our wavy simulations, the particle will eventually reach its preferred

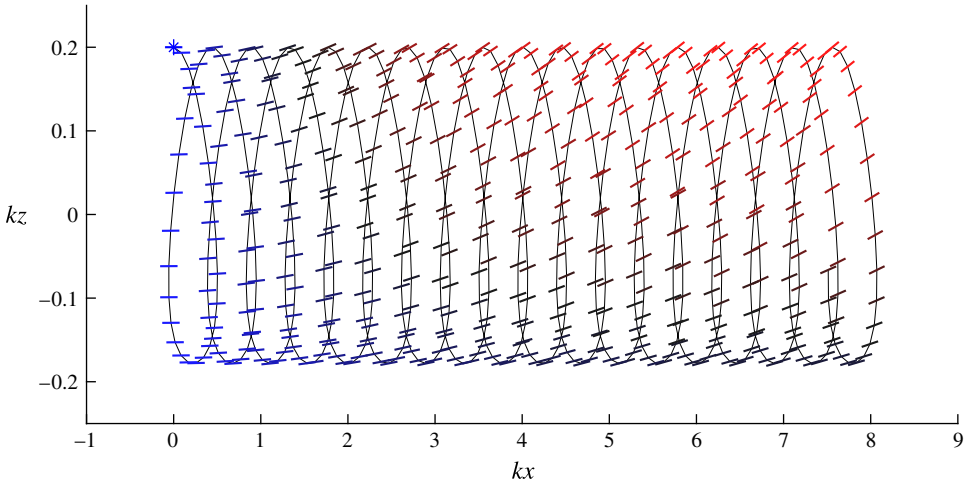

FIGURE 3. (Colour online) Spatial trajectory and orientation of an inertialess prolate particle over 18 wave periods, with $\mathcal{E} = 0.5$, and $kA = 0.2$. The black line represents the trajectory, and the marker lines are drawn, not to scale, along the particle's axis of symmetry, and are coloured by angle for emphasis. The particle has a net motion from left to right, with $*$ marking the starting position at $t = 0$.

alignment, although the time to reach this final alignment does depend on its initial condition. Due to the wavy nature of the flow, however, the particle will oscillate about its preferred alignment with the wave orbital period. This is shown in figure 3, where a non-inertial prolate spheroid with $\mathcal{E} = 0.5$ is initially oriented away from its preferred alignment in a wave field with $kA = 0.2$. As it translates, it rotates toward its preferred alignment; but this prolonged rotation is superimposed on a faster, back-and-forth oscillation coinciding with the wave orbital motion. By the end of the time span shown in figure 3, the particle has not yet reached its preferred alignment position; but once it does, it will continue to oscillate about it with all passing waves.

For all cases, even with out-of-plane initial orientations, the preferred alignment position of p_i is in the flow plane (x–z). We quantified this preferred alignment by measuring the steady-state T-averaged angle ϕ from the z-axis to the particle's x'-axis, where the polar angle $\phi = \cos^{-1}(p_3/\|\boldsymbol{p}\|)$ and $\|\boldsymbol{p}\| = 1$ in this case. As shown in figure 4, our results collapse for all flow cases and are solely a function of shape; indeed, we find that

$$\tan\phi = \lambda. \tag{3.1}$$

In the rod limit, the particle prefers to be horizontal, with its axis of symmetry pointed in the wave direction. In the disc limit, the particle's axis of symmetry is vertical. Both of these configurations minimize the particle cross-sectional area in the direction of mean flow. Thus, the preferred orientation may be a result of the particle minimizing its energy dissipation, akin to what Jeffery (1922) concluded from his orbit derivation. This finding could also be relevant to the preferred alignment found in wall turbulence by Challabotla, Zhao & Andersson (2015*b*), who found that rods align parallel to the wall and discs with their axis of symmetry normal to the wall.

No matter the initial condition, non-spherical particles in the inertialess limit will eventually align to their preferred orientation, as shown in figure 5. Unlike in the Jeffery orbit case, however, we find that the particles do not flip until the limits of

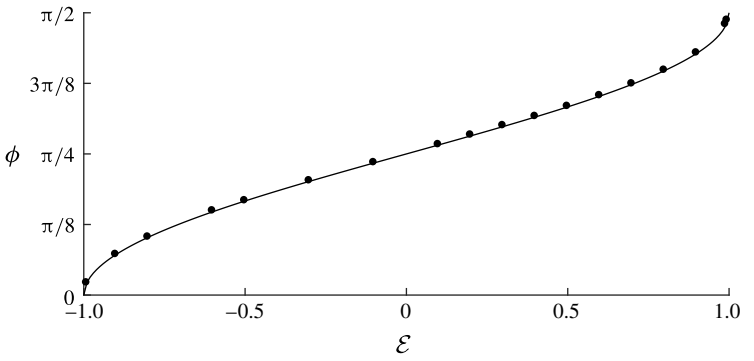

FIGURE 4. Polar angle ϕ for inertialess spheroids in wavy flow as a function of $\mathcal{E}$, showing the preferred alignment. The line shows (3.1), and the points are measured data from our simulations.

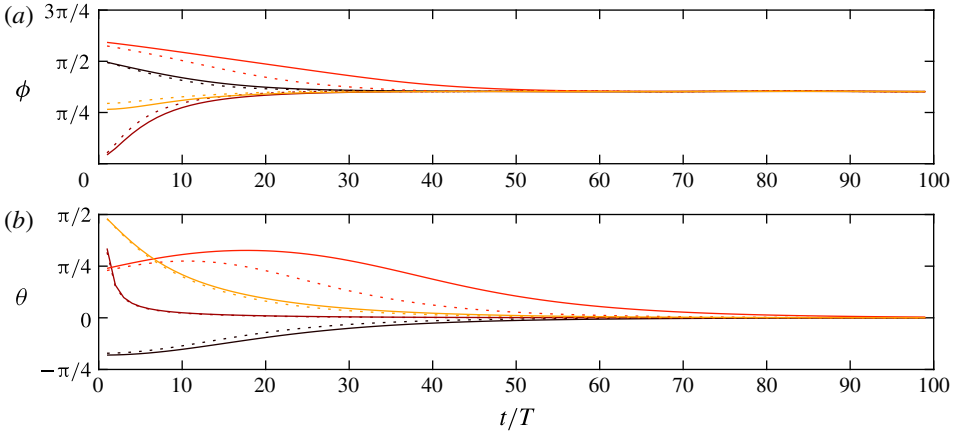

FIGURE 5. (Colour online) Wave-period-averaged orientation angles, for (*a*) polar angle ϕ, and (*b*) azimuthal angle θ, of particles started at different initial orientations in deep (solid) and shallow (dotted) water waves as a function of time normalized by wave period. All particles have $\mathcal{E} = 0.6$ and are inertialess. The colours correspond to different initial orientations. Oblate particles show similar results.

$\mathcal{E} \approx \pm 1$ are approached. We also find this mean alignment to be identical in all flows described by linear wave theory, including in the shallow-water limit also seen in figure 5. The mechanism that rotates the particle is solely due to the flow's shear. In linear waves, there is no mean shear. Instantaneously, however, deep-water waves do have shear in both the horizontal and vertical velocity components (that is, $\mathrm{d}u_x/\mathrm{d}z$ and $\mathrm{d}u_z/\mathrm{d}x$), and shallow-water waves have non-zero $\mathrm{d}u_z/\mathrm{d}x$. Furthermore, if one were to integrate the shear along the path of the particle to calculate a shear associated with the mean transport, it would only be non-zero for the deep-water case, and only in the $\mathrm{d}u_x/\mathrm{d}z$ component. Thus, we conclude that the unsteady shearing must be the feature of the flow that directs the particles to their alignment position, which is only a function of shape. We discuss this unsteadiness effect further below in § 3.4.

We still observe this alignment when inertia is introduced to the simulation; however, inertia slows down the rate at which the particles approach their final stable

orientation. As discussed further below, for example, negatively buoyant particles may settle below the wave field before they have had time to reach their preferred alignment. This can affect how to predict transport and dispersion of particle plumes.

3.2. *Mean transport*

In general, the rotational and translational degrees of freedom of symmetric particles like our spheroids are uncoupled (Brenner 1964); only particles without three symmetry planes will show coupling. However, in our case the flow itself provides the requisite symmetry breaking, and so the distinct preferred alignment of differently shaped particles becomes necessary information for predicting their mean transport. Thus, as compared with simple models of particle transport that simply superimpose a constant settling velocity on the fluid velocities, our model captures more of the complexity of particle transport by calculating both anisotropic added mass and drag forces.

The mean transport of non-neutrally buoyant, weakly inertial spherical particles under deep-water surface gravity waves was considered previously by Eames (2008). He defined the net transport, or the total horizontal distance travelled by a particle, as either the distance to where a negatively buoyant particle released at the surface settles below the wave field or a positively buoyant particle released below the wave field reaches the surface. We denote this horizontal displacement by X_∞. It is expected to be proportional to the wavelength multiplied by the ratio between the surface Stokes drift velocity u_s^0 and the particle settling velocity w_p (Eames 2008). For deep-water waves this prediction is expressed as

$$\frac{X_\infty}{L} = \frac{1}{4\pi}\frac{u_s^0}{|w_p|}. \tag{3.2}$$

This theory was derived for spherical particles, and in that case, the particles settling below waves do indeed asymptote to a measurable X_∞ value. However, as non-spherical particles descend and settle below the wave field, they can still continue to travel horizontally due to lift forces arising from their anisotropic drag, just like an anisotropic particle sedimenting in quiescent flow. Therefore, the value of X_∞ is sensitive to the depth chosen. Here, we define X_∞ for negatively buoyant particles in deep-water waves to be the total horizontal distance travelled from the time when the particles are released to the time when they have reached a depth at which the Stokes drift velocity has decayed to 1 % of its surface value. This occurs at a depth of $z_\infty = -0.37L$. Spherical particles have moved to within a fraction of a per cent of their asymptotic horizontal limit by the time they reach this depth. For positively buoyant particles, we take a similar approach: the particles are released at z_∞, and X_∞ is defined to be the point at which they reach the surface.

Depicted in figure 6 are the trajectories of both negatively (*a*) and positively buoyant (*b*) particles of different shapes with equal and opposite equivalent-sphere settling velocities; in other words, the settling velocity of the negatively buoyant particle in quiescent flow is equal and opposite to that of the rising velocity of its corresponding positively buoyant particle. We set this condition by fixing the particle size and shape and setting the particle density such that the settling velocities defined by (2.13) have the same magnitude but opposite sign. We present example trajectories in both cases of a sphere and a corresponding equivalently sized ellipsoid that is started in two different orientations; this demonstrates both the effects of

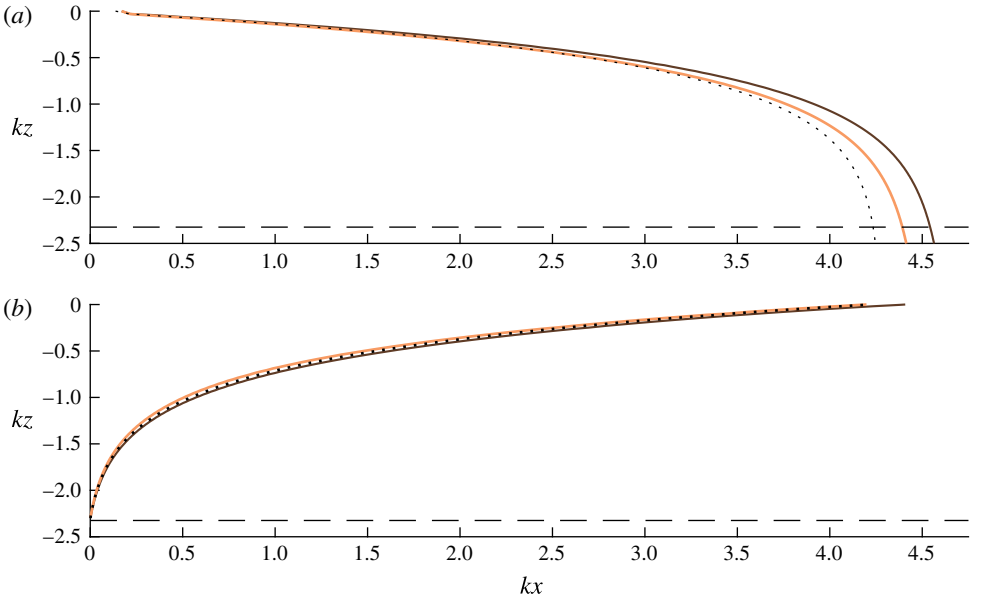

FIGURE 6. (Colour online) Trajectories of weakly inertial particles settling in deep-water waves. Wave-period-averaged trajectories of identical ellipsoidal particles with $\mathcal{E} = 0.5$ are marked with solid lines, those of an equivalent sphere with dotted lines and z_∞ is marked with dashed lines. Negatively buoyant particles ($\mathcal{B} = 0.99$) in (*a*) were started at the surface and positively buoyant particles ($\mathcal{B} = 1.01$) in (*b*) were started at z_∞ and stopped at the surface. All particles simulated have the same absolute equivalent-sphere settling velocity w_p^s. The waves have $kA = 0.15$. The ellipsoidal particles were started with different initial orientations in the x–z plane, as shown in figure 7; with $\phi = \pi/2, 0$. The time to X_∞ is (*a*) 146, 144 (*b*) 149, 138 wave periods for the ellipsoids, respectively, and it is 141 wave periods for spheres in both (*a*) and (*b*). While time to X_∞ varies across shape and orientation, the positively buoyant particles follow almost identical paths, whereas much more variation is seen in the negatively buoyant case. The results are similar for oblate particles.

shape and initial orientation. The spherical particles reach the same X_∞ value at the same time whether they are positively or negatively buoyant. This symmetry breaks, however, when the particles are anisotropic. This effect is entirely due to the vertical asymmetry in the flow; specifically, the vertical variation of the shear in the flow. The shear modulates each particle's rate of rotation and thus determines the differential resistance. Therefore the particles rotate much faster when started near the surface than when released far below it, as shown in figure 7, because the shear decreases exponentially with depth. This difference in particle rotation rate means that particles that begin high in the water column and sink adopt a different set of orientations, with respect to space and time, from those that begin lower in the water column and rise. This in turn means that the net drag on the rising and sinking particles is different, regardless of their initial orientations. These differences in drag lead to the asymmetry in transport we observe for anisotropic rising and falling particles. For particles on the surface itself, additional physical phenomena such as capillarity or other surface-tension effects or wave breaking may become important and contribute to the long-term transport. Since positively buoyant particles will eventually reach the

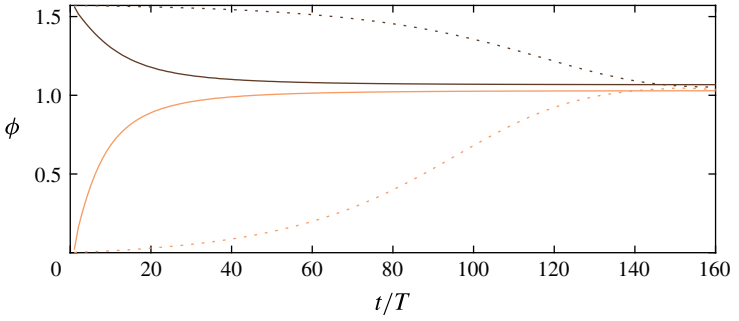

FIGURE 7. (Colour online) Wave-period-averaged polar angle ϕ of non-spherical particles in figure 6 over time. Solid lines indicate negatively buoyant and settling particles and dotted lines indicate positively buoyant and rising particles. Time is normalized by wave period. The particles have equal and opposite settling velocities.

surface even when released below it (unlike negatively buoyant particles), we therefore restrict the rest of our analysis to negatively buoyant particles only. However, we note that our results hold qualitatively for positively buoyant particles as well.

The initial orientation of a particle also affects its transport. In these non-stochastic simulations, all spherical particles will follow the same path. This is not true, however, for anisotropic particles, as shown clearly in figure 6: particles of the same (non-spherical) shape but started in different orientations follow different trajectories. To obtain a mean value of X_∞, we ran 1024 trials with initial orientations uniformly distributed on the unit sphere and averaged the results. Because of the axisymmetry of the particle, we only sample the ranges $0 \leqslant \phi < \pi$ and $0 \leqslant \theta < \pi/2$. Probability density functions (p.d.f.s) of the results are plotted in figure 8. In figure 8(*a*), the particle is much closer in shape to a sphere than in figure 8(*b*). Thus, there is significantly less variation in the trajectories, and the total width of the plume is much smaller. Significant skewness can be seen in the p.d.f.s as well, as will be explained later in this section. We note that out-of-plane motion is also captured in our simulations; however, it is orders of magnitude smaller than the horizontal motion, and so we neglect it in this analysis.

In addition to adding a finite width to the distribution of trajectories, we also find that non-spherical shape requires a re-evaluation of the prediction of X_∞ from (3.2). Although non-spherical particles do still follow the general trend of travelling further with increased Stokes drift velocity and shorter distances with increased absolute settling velocity, choosing how to define the settling velocity for a non-spherical particle is non-trivial. *A priori*, we can derive a settling velocity w_p^s based on the equivalent sphere in a quiescent fluid, a settling velocity based on the mean resistance tensor K_{ij} defined as $\overline{w_p}$, or a settling velocity based on the vertical resistance at the preferred alignment w_p^*. These three settling velocities are given by

$$w_p^s = \frac{g d_s^2 (\mathcal{B} - 1)}{18\nu}, \tag{3.3a}$$

$$\overline{w_p} = \frac{w_p^s}{\overline{K'}}, \tag{3.3b}$$

$$w_p^* = \frac{w_p^s}{K_{33}^*}. \tag{3.3c}$$

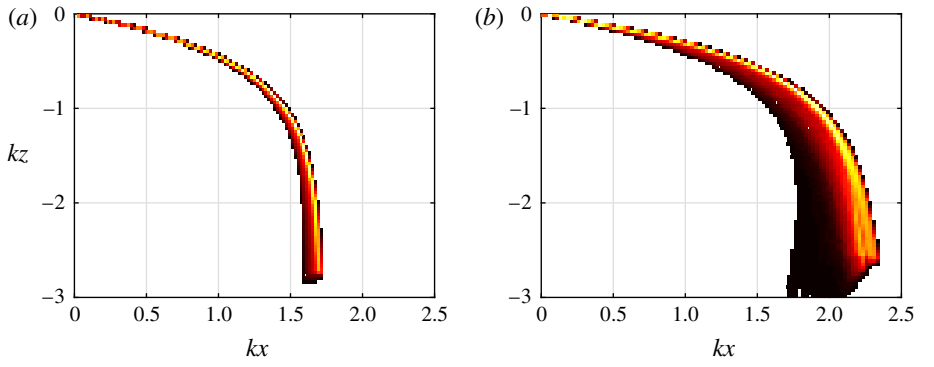

FIGURE 8. (Colour online) The p.d.f.s of particle trajectories with varied initial orientation. The histogram density goes from dark (fewest trajectories) to light (most). Both plots have identical kA, d_s and $\mathcal{B}$; panel (a), however, shows particles with $\mathcal{E} = 0.2$, and panel (b) shows particles with $\mathcal{E} = 0.9$.

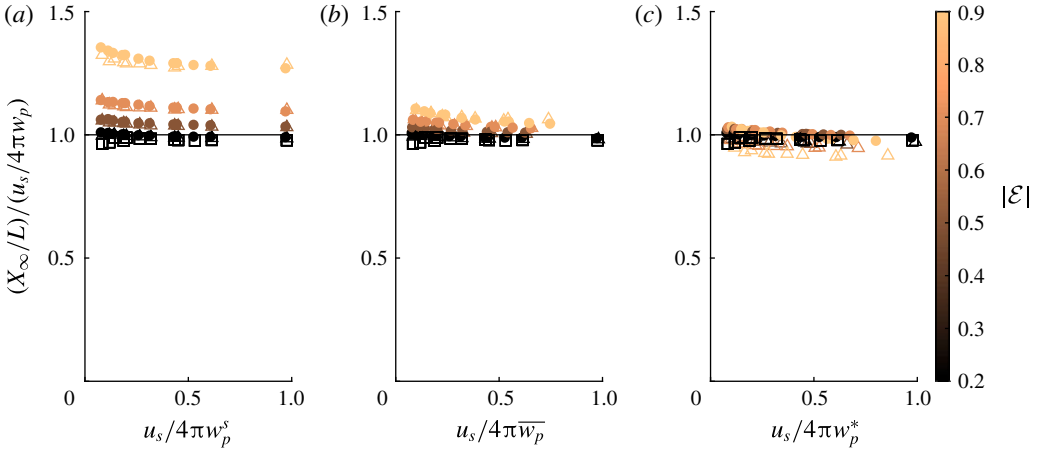

FIGURE 9. (Colour online) Tests of predicted horizontal transport for different settling velocity models. The relationship between X_∞/L and $u_s/4\pi w_p$ is plotted using compensated plots, where the former is normalized by the latter and plotted against it. The terms used for w_p are (a) w_p^s, (b) $\overline{w_p}$ and (c) w_p^*. The colour bar represents the absolute value of eccentricity, where triangles are oblate and circles are prolate. The square symbols are from simulations with spheres. These data are from trials with $kA = 0.15$.

Here, $\boldsymbol{K}^*$ is the resistance tensor in the basis aligned with the mean particle alignment and $\overline{K'}$ is the arithmetic mean of the eigenvalues of K_{ij} or equivalently the mean of the trace of K'.

We tested all of these velocities by inserting them into (3.2). As shown in figure 9, it is clear that the corrected settling velocities are better at predicting transport, with the w_p^* formulation in figure 9(c) having an R^2 value of 0.997. If there were no preferred alignment for the particles, if they were randomly oriented in space at all times, then the mean particle transport averaged over all initial orientations would follow the prediction using $\overline{w_p}$. But this assumption results in an under-prediction of

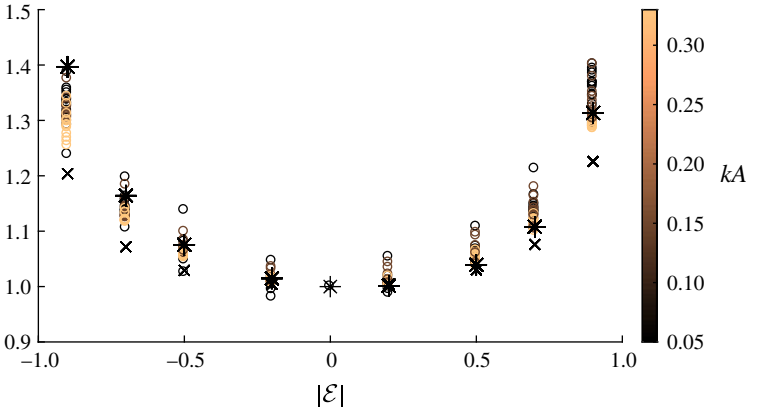

FIGURE 10. (Colour online) Mean horizontal transport X_∞ of a negatively buoyant non-spherical particle normalized by the transport of its equivalent sphere, shown as $\circ$, plotted against eccentricity. The isotropic mean resistance tensor eigenvalue $\overline{K'}$ is plotted as $\times$, and the preferred alignment vertical resistance K^*_{33} is denoted by $*$. The colour bar represents wave steepness kA.

transport, as shown in figure 10. This can also be seen in figure 8, where the highest density of trajectories in the p.d.f. is skewed farther downstream than the centre of the plume; thus, the preferential alignment is responsible for this skewness. Shape is also important, and this variation with eccentricity is also shown in figure 10. The preferred alignment resistance, K^*_{33}, corresponds with the trends in normalized transport with eccentricity better than the isotropic resistance value $\overline{K'}$. Therefore, the random orientation prediction using $\overline{w_p}$ both underperforms the w^*_p prediction and underestimates the transport. The preferred alignment must enhance vertical drag on the particle, thus minimizing average settling velocities and allowing the particle to be transported farther before it settles below the wave field. There is also a trend with wave steepness, in that anisotropic particles in less steep waves travel farther than in steeper waves. Furthermore, we note that the mean horizontal transport of a spheroid can be almost 1.5 times greater than the transport of an equivalent spherical particle. Thus, as argued above, the effects of both shape and alignment must be included when predicting transport.

3.3. *Dispersion*

As we have shown, varying only the initial orientation of the particles can have a measurable impact on total transport. By running simulations across a range of initial orientations while keeping all other physical particle and flow parameters constant, we can characterize the evolution of a plume of released particles. First, let us note that neither anisotropic-particle shape nor inertia alone can cause dispersion in our simulations; both are needed. Without the former, there will be no difference between the trajectories of particles released with different initial orientations; and without the latter, the particles reduce to fluid tracers, in terms of their transport.

We uniformly sampled the space of unique three-dimensional initial orientations (disregarding those where symmetry of the particle or of the flow dictates identical results) for 1024 different values of $p_i(t = 0)$. We find that horizontal dispersion, defined as $\sigma_{X\infty}$, the standard deviation of X_∞, increases with greater absolute particle

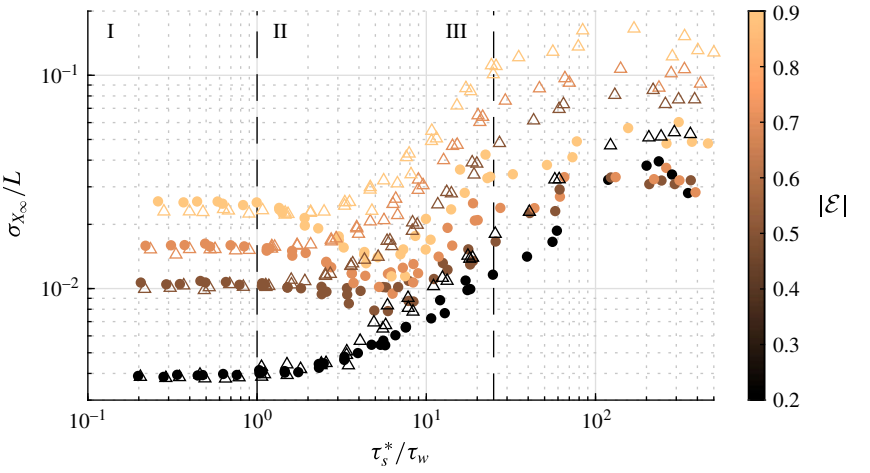

FIGURE 11. (Colour online) Horizontal dispersion of negatively buoyant particle plumes, plotted as the standard deviation of normalized X_∞ against a ratio of time scales. The symbol $\triangle$ is for oblate, and $\bullet$ for prolate. Colour bar values indicate absolute eccentricity. The figure is broken into three regimes. Data come from trials with varied kA and St.

eccentricity. Also, while inertia is necessary for dispersion to occur, it can also suppress dispersion. As particles become too heavy, they may settle out of the wave field before they have the chance to disperse. This settling is controlled by the general settling time scale $\tau_s = L/w_p$. The transport of the particles is determined by the magnitude of the Stokes drift velocity u_s (2.12), from which we can define a wave transport time scale $\tau_w = L/u_s^0$ using its value at the surface and the wavelength. A settling time scale $\tau_s^* = L/w_p^*$ based on the preferred alignment can also be defined. Thus, u_s/w_s^* can be rewritten as τ_s^*/τ_w, which allows us to express the physics controlling the phenomena as a ratio of two competing time scales. This normalization collapses the data for $\sigma_{X\infty}$ into three distinct regimes, which we label as I, II and III in figure 11. We refer to these regimes as the settling, dispersive and aligned regimes, respectively.

In the settling regime, $\tau_w > \tau_s^*$. Here, the particles settle out of the wave field before they have a chance to be transported horizontally. They do not remain in the water column long enough for significant dispersion to take place, so whatever dispersion they do feel is due to various initial-condition-dependent lift forces on the particle as they sediment.

Once τ_w and τ_s^* are of the same order, the dispersion data deviate from the flat distributions seen in the settling regime and enters the dispersive regime. Here, the $\sigma_{x\infty}$ values of the oblate particle plumes increase monotonically with τ_s^*/τ_w. This occurs because the particles are transported through the wave field for a longer distance before they settle out. If solely examining the oblate particle results, one would conclude that the larger τ_s^*/τ_w ratios within this regime are indicative of more dispersion. However, for some of the prolate particles, the relationship is more complicated. For high-eccentricity prolate particles ($\mathcal{E} > 0.2$), dispersion in fact decreases at the onset of the dispersive regime. This is due to the fact that the particles are starting to align. The rate at which the particles align is not constant, as seen in figure 7; and in fact, the rate at which they align decreases over time. Therefore, the particles first quickly align to similar orientations, resulting in similar

forcing on the particle and suppressing the dispersion. This bulk alignment rate is very different for oblate and prolate particles due to their different moments of inertia. Prolate particles are all almost aligned as they move through the dispersive regime, although some variability in their orientations still remains; thus, the dispersion is not removed but rather only slowed and is able to grow again at larger τ_s^*/τ_w values. Oblate particles, on the other hand, have a much broader distribution of orientations, and their dispersion is stronger.

Finally, in the aligned regime, the particles have been in the waves long enough that they have all reached their preferred alignment. At this point, the dispersion ceases to grow, since the mechanism that drives it has been removed.

Our results demonstrate that the more anisotropic the particle, the more dispersion will be observed. But we also find that oblate ellipsoids disperse much more than their prolate counterparts. And, in general, more dispersion occurs when the transport is strong compared to the particle settling, or equivalently when the wave transport time scale is much shorter than the settling time scale. Furthermore, while there is a mechanism for dispersion in these simulations, we have demonstrated that the particles do not disperse without bound – in other words, if one were to predict that the anisotropic particles do not align and instead persist in random orientations, one would over-predict particle dispersion.

3.4. *Effects of waviness*

So far, our discussion has focused primarily on the properties of the Stokes drift rather than on the waves themselves. But the effect of the waves is not unimportant for the mean transport and dispersion of the particles. Here, we define the 'waviness' as the unsteady oscillating component of the flow. We isolate the effects of the waviness on transport by repeating the simulations using only the residual Stokes drift velocity field. This leads to a steady shear flow that decays exponentially with depth, described by (2.12). Note that this flow is no longer irrotational.

In a steady creeping shear flow, the particles undergo the expected Jeffery orbits. This is clearly seen when the particles from figure 5 were evolved in the deep-water residual Stokes drift velocity field alone. We show the corresponding orientation as a function of time in figure 12. Each particle undergoes a three-dimensional periodic orbit. The period is the same in all cases, as it is solely a function of the shear rate and aspect ratio. However, the type of orbit is dependent on initial orientation. The period of the orbits, as derived by Jeffery (1922), is $2\pi(\lambda + 1/\lambda)/\dot{\gamma}$ where $\dot{\gamma}$ is the shear rate.

When negatively buoyant particles are evolved in this type of flow, we can measure the new X_∞ and $\sigma_{x\infty}$ values and compare to the corresponding wavy cases. We find that there is a measurable difference in both dispersion and mean transport of the particles. This makes sense, as we have already confirmed that orientational drag is important for transport; therefore, variations in particle orientation should affect the mean transport. In the presence of waves, the particle plumes tend to disperse more, but there is less mean transport. Particles in the Settling regime have identical plume dispersion with or without the wavy flow, but particles in the dispersive and aligned regime all have more dispersion in waves, with $\sigma_{x\infty}$ in some cases more than an order of magnitude higher. However, there is no clear trend indicating what controls this deviation. The mean transport is up to 30 % higher in the residual flow case. These results indicate that there remains much to be learned about the detailed effects of waves on particle transport.

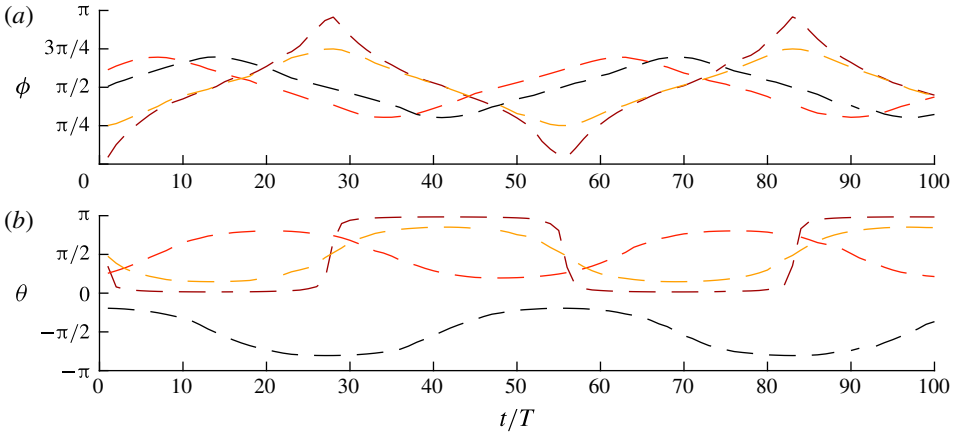

FIGURE 12. (Colour online) Orientation of identical prolate spheroids as a function of time in the same residual wave field with various initial orientations. The various colours represent corresponding orientation angles, for (*a*) polar angle ϕ and (*b*) azimuthal angle θ for particles started with different initial orientations in a deep-water residual Stokes drift velocity field as a function of time normalized by wave period. All particles have $\mathcal{E} = 0.6$ and are inertialess. All oblate and prolate particles undergo similar orbits.

4. Discussion and conclusions

To summarize our results, we conducted simulations of particle transport under linear surface gravity waves, extending previous work on this problem by incorporating the effects of particle anisotropy. We found that both prolate and oblate spheroids show preferred orientations, even without particle inertia. This alignment persists when the particles have weak inertia and must be considered when computing the particle's mean settling velocity and transport. We also demonstrated that particle anisotropy causes the dispersion of particle plumes released with different initial orientations. Moreover, this dispersion cannot grow indefinitely as the particles will all eventually align if in the water column long enough. The unsteady shearing in waves both qualitatively and quantitatively affects how the particles are oriented and transported. Finally, our results suggest that the non-dimensional parameter that best describes the transport of weakly inertial anisotropic particles in wavy flows is not St or Re_p but rather the velocity ratio u_s/w_p^*. This ratio captures the relative importance of the wave steepness kA, which corresponds to the amount of shear in the flow, and St, which captures the drag as the particle settles out of the wave field, as well as the preferred particle orientation.

Even though our simulations have revealed many features of the dynamics of spheroidal particles in wavy flows, there are many aspects that we have certainly not fully captured and that warrant further study. For example, we have assumed drag laws and torques that are only exact in the Stokes flow regime, where $Re_p \ll 1$. The drag coefficients vary as Re_p increases above unity, and as Re_p grows past approximately 22, the laminar wakes of the particles may detach, and the drag should be re-parameterized (Zastawny *et al.* 2012). Nevertheless, although the specifics of the drag coefficients will change in this intermediate Re_p regime, the anisotropy of the drag forces, as well as the variation for different eccentricities, will remain (Ouchene *et al.* 2016); and, as we have shown, the underlying physical mechanism for the effects we have observed is this anisotropic drag coupled with the dynamics of the

flow field. The torques on the particle will be dependent on a rotational Reynolds number based on the particle's length scale and angular velocity. Although the details of how Reynolds-number-dependent torques will affect our results are not clear at this time, the relationship between angle of attack and eccentricity will remain at increased Reynolds number (Ouchene *et al.* 2016). Thus, although we would expect our results to change quantitatively with a different assumed drag law and torque parameterization, the same qualitative effects seen should still hold with increased particle inertia.

We have also shown that the specific nature of the flow field matters in determining the particle transport, since we find qualitatively different results when considering full wavy flows or only the residual shear component. We have not, however, studied the effects of turbulence, which may affect the preferred particle orientation we have observed. For example, there exists a limit when the effects of turbulence outweigh those of the waves, where the particles react as if they were subjected to turbulence alone. However, weaker turbulence will likely introduce a stochastic component to the particle motion while not necessarily destroying the preferential orientation. We leave these questions for more detailed numerical simulations or laboratory experiments.

Finally, while we have primarily considered negatively buoyant particles here, the same ideas apply to positively buoyant particles. However, since the shear rotating the particles is much weaker at depth in wavy flows, the quantitative results may be somewhat different. Furthermore, once the particles reach the surface, other forces may become important, affecting the long-term transport of positively buoyant particles in additional ways. We anticipate that this will be a fruitful area of study.

Acknowledgements

M.H.D. gratefully acknowledges the support of the Stanford Graduate Fellowship. This work was supported by the US National Science Foundation under grant no. CBET-1706586.

REFERENCES

ANDERSSON, H. I. & SOLDATI, A. 2013 Anisotropic particles in turbulence: status and outlook. *Acta Mechanica* **224**, 2219–2223.

BAKHODAY-PASKYABI, M. 2015 Particle motions beneath irrotational water waves. *Ocean Dyn.* **65**, 1063–1078.

BERON-VERA, F. J., OLASCOAGA, M. J. & LUMPKIN, R. 2016 Inertia-induced accumulation of flotsam in the subtropical gyres. *Geophys. Res. Lett.* **43**, 12228–12233.

BRENNER, H. 1964 The Stokes resistance of an arbitrary particle II: an extension. *Chem. Engng Sci.* **19**, 599–629.

BRETHERTON, F. P. 1962 The motion of rigid particles in a shear flow at low Reynolds number. *J. Fluid Mech.* **14**, 284–304.

BRODAY, D., FICHMAN, M., SHAPIRO, M. & GUTFINGER, C. 1997 Motion of diffusionless particles in vertical stagnation flows II. Deposition efficiency of elongated particles. *J. Aero. Sci.* **28**, 35–52.

BYRON, M., EINARSSON, J., GUSTAVSSON, K., VOTH, G., MEHLIG, B. & VARIANO, E. 2015 Shape-dependence of particle rotation in isotropic turbulence. *Phys. Fluids* **27**, 035101.

CHALLABOTLA, N. R., ZHAO, L. & ANDERSSON, H. I. 2015*a* Orientation and rotation of inertial disk particles in wall turbulence. *J. Fluid Mech.* **766**, R2.

CHALLABOTLA, N. R., ZHAO, L. & ANDERSSON, H. I. 2015*b* Shape effects on dynamics of inertia-free spheroids in wall turbulence. *Phys. Fluids* **27**, 061703.

CHUBARENKO, I., BAGAEV, A., ZOBKOV, M. & ESIUKOVA, E. 2016 On some physical and dynamical properties of microplastic particles in marine environment. *Mar. Pollut. Bull.* **108**, 105–112.

EAMES, I. 2008 Settling of particles beneath water waves. *J. Phys. Oceanogr.* **38**, 2846–2853.

EINARSSON, J., ANGILELLA, J. R. & MEHLIG, B. 2014 Orientational dynamics of weakly inertial axisymmetric particles in steady viscous flows. *Physica* D **278**, 79–85.

GALLILY, I. & COHEN, A. H. 1979 On the orderly nature of the motion of nonspherical aerosol particles. ii. inertial collision between a spherical large droplet and an axially symmetrical elongated particle. *J. Colloid Interface Sci.* **68**, 338–356.

GRINSHPUN, S. A., REDCOBORODY, Y. N., KRAVCHUK, S. G., ZADOROZHNII, V. I. & ZHDANOV, V. I. 2000 Particle drift in the field of internal gravity wave. *Intl J. Multiphase Flow* **26**, 1305–1324.

GUHA, A. 2008 Transport and deposition of particles in turbulent and laminar flow. *Annu. Rev. Fluid Mech.* **40**, 311–341.

HASSELMANN, K. 1970 Wave driven inertial oscillations. *Geophys. Fluid Dyn.* **1**, 463–502.

ISOBE, A., KUBO, K., TAMURA, Y., KAKO, S., NAKASHIMA, E. & FUJII, N. 2014 Selective transport of microplastics and mesoplastics by drifting in coastal waters. *Mar. Pollut. Bull.* **89**, 324–330.

JANSONS, K. M. & LYTHE, G. D. 1998 Stochastic Stokes drift. *Phys. Rev. Lett.* **81**, 3136–3139.

JEFFERY, G. B. 1922 The motion of ellipsoidal particles imnmersed in a viscous fluid. *Proc. R. Soc. Lond.* A **102**, 161–179.

KLETT, J. D. 1995 Orientation model for particles in turbulence. *J. Atmos. Sci.* **52**, 2276–2285.

KUKULKA, T., PROSKUROWSKI, G., MORÉT-FERGUSON, S., MEYER, D. W. & LAW, K. L. 2012 The effect of wind mixing on the vertical distribution of buoyant plastic debris. *Geophys. Res. Lett.* **39**, L07601.

LAMB, H. 1945 *Hydrodynamics*, 6th edn. Dover.

LEAL, L. G. 1980 Particle motions in a viscous fluid. *Annu. Rev. Fluid Mech.* **12**, 435–476.

LEIBOVICH, S. 1983 The form and dynamics of Langmuir circulations. *Annu. Rev. Fluid Mech.* **15**, 391–427.

LING, Y., PARMAR, M. & BALACHANDAR, S. 2013 A scaling analysis of added-mass and history forces and their coupling in dispersed multiphase flows. *Intl J. Multiphase Flow* **57**, 102–114.

LOTH, E. 2008 Drag of non-spherical solid particles of regular and irregular shape. *Powder Technol.* **182**, 342–353.

MAXEY, M. R. & RILEY, J. J. 1983 Equation of motion for a small rigid sphere in a nonuniform flow. *Phys. Fluids* **26**, 883–889.

MAXIMENKO, N., HAFNER, J. & NIILER, P. 2012 Pathways of marine debris derived from trajectories of Lagrangian drifters. *Mar. Pollut. Bull.* **65**, 51–62.

MCWILLIAMS, J. C., SULLIVAN, P. P. & MOENG, C. 1997 Langmuir turbulence in the ocean. *J. Fluid Mech.* **334**, 1–30.

MORTENSEN, P. H., ANDERSSON, H. I., GILLISSEN, J. J. J. & BOERSMA, B. J. 2008 Dynamics of prolate ellipsoidal particles in a turbulent channel flow. *Phys. Fluids* **20**, 093302.

NI, R., OUELLETTE, N. T. & VOTH, G. A. 2014 Alignment of vorticity and rods with Lagrangian fluid stretching in turbulence. *J. Fluid Mech.* **743**, R3.

OBERBECK, A. 1876 Über stationäre Flüssigkeitsbewegungen mit Berücksichtigung der inneren Reibung. *J. Reine Angew. Math.* **81**, 62–80.

OUCHENE, R., KHALIJ, M., ARCEN, B. & TANIÈRE, A. 2016 A new set of correlations of drag, lift and torque coefficients for non-spherical particles and large Reynolds numbers. *Powder Technol.* **303**, 33–43.

OUELLETTE, N. T., O'MALLEY, P. J. J. & GOLLUB, J. P. 2008 Transport of finite-sized particles in chaotic flow. *Phys. Rev. Lett.* **101**, 174504.

PARSA, S., CALZAVARINI, E., TOSCHI, F. & VOTH, G. A. 2012 Rotation rate of rods in turbulent fluid flow. *Phys. Rev. Lett.* **109**, 134501.

PUMIR, A. & WILKINSON, M. 2011 Orientation statistics of small particles in turbulence. *New J. Phys.* **13**, 093030.

RYAN, P. G., MOORE, C. J., VAN FRANEKER, J. A. & MOLONEY, C. L. 2009 Monitoring the abundance of plastic debris in the marine environment. *Phil. Trans. R. Soc. Lond.* B **364**, 1999–2012.

SANTAMARIA, F., BOFFETTA, G., AFONSO, M. M., MAZZINO, A., ONORATO, M. & PUGLIESE, D. 2013 Stokes drift for inertial particles transported by water waves. *Europhys. Lett.* **102**, 14003.

SHAPIRO, M. & GOLDENBERG, M. 1993 Deposition of glass fiber particles from turbulent air flow in a pipe. *J. Aero. Sci.* **24**, 65–87.

SHIN, M. & KOCH, D. L. 2005 Rotational and translational dispersion of fibres in isotropic turbulent flows. *J. Fluid Mech.* **540**, 143–173.

SIEWERT, C., KUNNEN, R. P. J., MEINKE, M. & SCHRÖDER, W. 2014 Orientation statistics and settling velocity of ellipsoids in decaying turbulence. *Atmos. Res.* **142**, 45–56.

STOKES, G. G. 1851 On the effect of the internal friction of fluids on the motion of pendulums. *Trans. Camb. Phil. Soc.* **9**, 8–106.

VAN SEBILLE, E., WILCOX, C., LEBRETON, L., MAXIMENKO, N., HARDESTY, B. D., VAN FRANEKER, J. A., ERIKSEN, M., SIEGEL, D., GALGANI, F. & LAW, K. L. 2015 A global inventory of small floating plastic debris. *Environ. Res. Lett.* **10**, 124006.

VOTH, G. A. & SOLDATI, A. 2017 Anisotropic particles in turbulence. *Annu. Rev. Fluid Mech.* **49**, 249–276.

ZASTAWNY, M., MALLOUPPAS, G., ZHAO, F. & VAN WACHEM, B. 2012 Derivation of drag and lift force and torque coefficients for non-spherical particles in flows. *Intl J. Multiphase Flow* **39**, 227–239.

ZHAO, L., CHALLABOTLA, N. R., ANDERSSON, H. I. & VARIANO, E. A. 2015 Rotation of nonspherical particles in turbulent channel flow. *Phys. Rev. Lett.* **115**, 244501.